

Diagnosis scheme for topological degeneracies crossing high-symmetry lines

Tiantian Zhang^{1,2,3,*}, Ling Lu,^{1,4} Shuichi Murakami^{2,3}, Zhong Fang,^{1,5} Hongming Weng^{1,5,†} and Chen Fang^{1,6,‡}

¹*Institute of Physics, Chinese Academy of Sciences/Beijing National Laboratory for Condensed Matter Physics, Beijing 100190, China*

²*Department of Physics, Tokyo Institute of Technology, Ookayama, Meguro-ku, Tokyo 152-8551, Japan*

³*Tokodai Institute for Element Strategy, Tokyo Institute of Technology, Nagatsuta, Midori-ku, Yokohama, Kanagawa 226-8503, Japan*

⁴*Songshan Lake Materials Laboratory, Dongguan, Guangdong 523808, China*

⁵*Collaborative Innovation Center of Quantum Matter, Beijing 100084, China*

⁶*CAS Center for Excellence in Topological Quantum Computation, Beijing 100190, China*



(Received 24 November 2019; accepted 3 June 2020; published 23 June 2020)

Theories of symmetry-based indicators and topological quantum chemistry, while powerful in diagnosing gapped topological materials, cannot be directly applied to diagnosing band degeneracies at/between high-symmetry momenta due to the violation of the compatibility conditions. However, the only information that compatibility condition can tell us is whether there are band degeneracies at/between high-symmetry momenta or not. Here we design a recursive protocol that utilizes indicators of maximal subgroups to infer the topological information of band degeneracies crossing high-symmetry lines without implementing a heavy numerical calculation, such as the existence, type, number, configuration for the band degeneracies, and so on. For demonstration, the method is used to predict the existence of ideal Weyl phonons in In_2Te and node-cage phonons in ZrSiO , respectively.

DOI: [10.1103/PhysRevResearch.2.022066](https://doi.org/10.1103/PhysRevResearch.2.022066)

Introduction. Theories of symmetry-based indicators [1] and topological quantum chemistry [2] are useful in diagnosing topological materials, such as topological insulators [3,4], topological crystalline insulators [5], and topological semimetals [6]. However, the application of those theories needs to meet one condition, i.e., compatibility condition, which restricts the number of each irreducible representation for the occupied band at several high-symmetry points (HSPs) in the Brillouin zone (BZ). When the condition is satisfied, there will be no band crossings at/between HSPs, as shown in Fig. 1(a), or band crossings along high-symmetry lines (HSLs) can be gapped without changing the order of bands between the occupied bands and unoccupied bands at HSPs (see the Supplemental Material for details [7]). Among the cataloged topological materials, topological semimetals diagnosed by the compatibility condition are the majority, which is more than 62% in the spinful case and 98% in the “spinless” case (ignoring spin-orbit coupling) [8–10], corresponding to the case in Fig. 1(b). For such huge amounts of topological semimetals, the only information that the previous work tells us is whether the topological degeneracy is at a HSP or along a HSL. Other topological information, such as the type, number, configuration, and positions for the topological degeneracies

are missed. The incomplete information for the topological degeneracies is due to the imperfect algorithm in the previous work. Therefore, a method to diagnose whole information for such topological degeneracies is highly deserved.

The importance of such information, however, is highlighted in the research of topological semimetals, such as Weyl semimetals [11–15], Dirac semimetals [16–19], and node-line semimetals [20,21]. The nontrivial topology of band degeneracies in some of these materials leads to unique surface states having “Fermi arcs” [22–25] as well as an anomalous bulk transport phenomenon known as the “quantum anomaly” [26–30]. Topologically nontrivial band degeneracies appear not only in electronic bands but are also predicted and observed in the bands of bosons such as photons [25,31–33], phonons [34–48], and magnons [49,50].

In this Rapid Communication, we develop a routine for topological-diagnosing band degeneracies located along high-symmetry lines in the BZ, which can be used in both spinful and spinless systems with/without time-reversal symmetry. In the following, we will discuss our algorithm in AI class systems as an example, which corresponds to orthogonal Hamiltonians [51–53]. (Discussions on spinful systems are in the Supplemental Material [7].) Given a band structure that violates the compatibility conditions of some space group G , we first identify, through a “tree-search” process, the maximum subgroup $H \subset G$, such that the compatibility conditions of H are satisfied, and then compute the symmetry-based indicators with respect to H . The value of the symmetry-based indicator for this subgroup then reveals partial information on topological invariants of the band degeneracies protected by G , which has not been discussed in detail before [6,9,10]. For example, the lowest six phonon bands of In_2Te violate the compatibility conditions of #216. Figure 1(c) shows all

*zhang.t.ac@m.titech.ac.jp

†hmweng@iphy.ac.cn

‡cfang@iphy.ac.cn

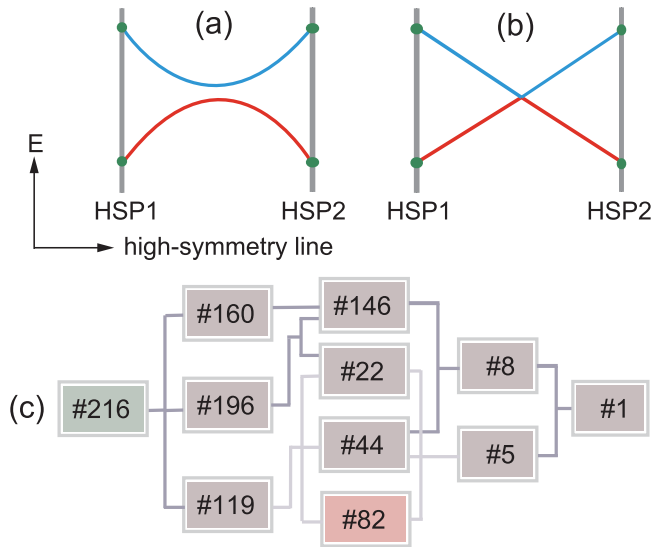


FIG. 1. (a) and (b) show two different kinds of band structure along a high-symmetry line. The red line represents the occupied band, and the blue line represents the unoccupied band. HSP1 and HSP2 represent two different high-symmetry points in the Brillouin zone. The band structure in (a) satisfies the compatibility condition, while (b) does not. (c) shows the tree-search process for #216, which is the key step in our diagnosis algorithm. #82 is the only maximum subgroup which has a nontrivial symmetry-based indicator and satisfies the compatibility condition for the lowest six phonon bands of In_2Te .

subgroups of space group #216, from which we identify #82 as the maximum subgroup that has nontrivial indicator group (\mathbb{Z}_2) and satisfies the compatibility condition at the same time. We then compute the \mathbb{Z}_2 indicator for #82 and find $z_2 = 1$, which by Ref. [6] ensures that the band degeneracies between the sixth and the seventh bands are Weyl points of equal energy. We also apply the method to the phonon bands of ZrSiO and show the presence of a “nodal cage” in its band structure.

Flowchart for the recursive algorithm. The diagnosing process for topological degeneracies in the Brillouin zone is summarized in Fig. 2(a), which consists of five steps. In step I, symmetry data, i.e., irreducible representation, at a given list of high-symmetry momenta should be calculated by first-principles calculations. In step II, analyze if two conditions, i.e., the nontrivial-symmetry-based-indicator-group condition (INDC) and compatibility condition (CC) are satisfied by the space group and the symmetry data, respectively. If INDC and CC are both satisfied, which corresponds to “YY” in the flowchart, then we can calculate the symmetry-based indicator directly by Ref. [6] to get the information of topological band degeneracies at generic momenta in the BZ. If INDC is not satisfied while CC is, which corresponds to “NY” in the flowchart, then the system is in a “trivial” state. (Here “trivial” means that of an atomic insulator, i.e., band degeneracies in the Brillouin zone, can be gapped out without changing the order of bands between the occupied bands and unoccupied bands at high-symmetry momenta.) In other cases, CC is not satisfied, i.e., band degeneracies will exist at high-symmetry points or along high-symmetry lines, so we should use a new

method to diagnose the information for band crossings in the BZ. In step III, we find all the maximal subgroups of G , and choose one subgroup H from this set, and test if the INDC and CC are satisfied: If the answer is YY, we proceed to step IV; if the answer is others, we replace H by its lower subgroups to repeat the recursive process step III, until we get an answer of YY or the subgroup is #1. In step IV, we should use the symmetry-based indicator formula of H to diagnose the topological degeneracy information of space group G , no matter whether the indicator is zero or not. In step V, the indicator of the subgroup H can tell us the information of topological degeneracies crossing high-symmetry lines, such as types, configuration, positions, and topological charge for the topological degeneracies in the BZ. If the process stops at #1 in step IV, we conclude that the nodes cannot be further diagnosed by eigenvalues at all (nondiagnosable). After the process, each band node protected by G is to be found either as nondiagnosable, or as having a list of subgroups with corresponding indicators, which carry topological information on these nodes.

Figure 2 also lists two materials for the demonstration of our recursive algorithm in phononic systems. Figure 2(b) is an example of In_2Te , which has a noncentrosymmetric structure and 12 ideal Weyl points in the phonon spectra. Figure 2(c) is an example of ZrSiO , which has a centrosymmetric structure and nodal cage band degeneracies in the phonon spectrum. Both of the cases break CC in step II.

Diagnosing process for ideal Weyl phonons in In_2Te . In_2Te belongs to a \mathcal{P} -broken space group $F\bar{4}3m$ (#216) [54], as shown in Fig. 3(a). The band crossing at around 3.22 THz (E_w) indicates that CC is broken along the X - W direction for the lowest six bands, as shown in Fig. 3(e). In the following, we will get the complete information for the band crossing at around 3.22 THz by using the diagnosing method shown in Fig. 2(a).

After obtaining symmetry data for #216 in step I [55,56], we notice that CC for #216 is not satisfied along the X - W direction, which is not a surprise because of the band crossing in phonon spectra. However, there is not a nontrivial indicator for space group #216 in step II. Therefore in step III, we map each irreducible representation from #216 to #82 (I_4), which is the maximum subgroup both having a nontrivial indicator \mathbb{Z}_2 and satisfying CC. In step IV, we calculate the topological invariant of subgroup #82 and get a nonzero indicator $z_2 = 1$, which indicates that there will be 4 mod 8 Weyl points on the $k_z = 0$ plane (which is also the $k_3 = 0$ plane) between the sixth and seventh bands. In the following, we will provide an intuitive perspective to understand how to get the complete information for the topological degeneracies at high-symmetry momenta for #216 from the indicator of the subgroup #82.

Figure 3(c) shows the BZ for space group #82, which has a similar shape with the one for #216 shown in Fig. 3(b). Since there are two pieces of plane for the $k_3 = 0$ plane in Fig. 3(c), we can rebuild the BZ by dividing the blue quadrilateral plane into four pieces and fill them into the pink plane separately to get a new quadrilateral $k_3 = 0$ plane. In this case, the high-symmetry point M_1 in the old BZ is M_2 in the new BZ. Since there are 4 mod 8 Weyl points on the $k_1 = 0$ plane, shown by red and green dots in Fig. 3(c), we find that there will be

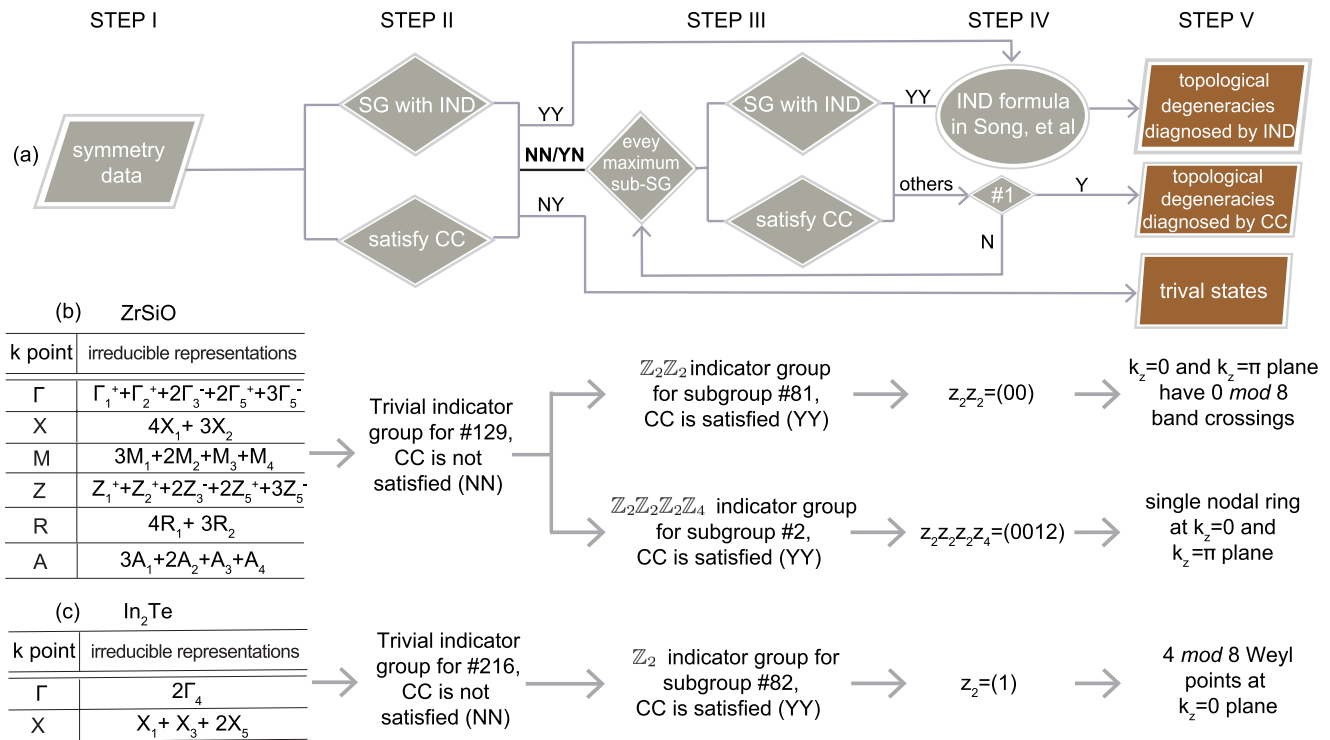


FIG. 2. (a) Calculation steps for diagnosing topological degeneracies in the Brillouin zone. SG: space group; IND: indicator; CC: compatibility condition; N: No; Y: Yes. Firstly, obtain the symmetry data by first-principles calculations, and feed them into the next step. Secondly, check whether the space group G has a nontrivial indicator and whether the symmetry data satisfies compatibility conditions. If both the answers are yes, we can use the symmetry data to calculate the indicator directly and get the information of topological degeneracies at generic momenta for AI class systems. If the answers are “NY,” which corresponds to the condition of “No” to “space group with nontrivial symmetry-based indicator” and “Yes” to “satisfy compatibility condition,” the material is a topologically trivial one, i.e., no topological degeneracies exist in the Brillouin zone. Otherwise, topological degeneracies will exist at high-symmetry momenta, such as high-symmetry points and high-symmetry lines. Thirdly, we should find all the maximum subgroups H which have a nontrivial symmetry-based indicator group and satisfy the compatibility condition at the same time in the tree-search process. After calculating the symmetry-based indicator for each maximum subgroup H in step IV, we can get information of topological degeneracies for space group G . However, if we cannot find a subgroup H in step III, then the topological degeneracies only can be diagnosed by compatibility condition. (b) In₂Te and (c) ZrSiO are two examples for demonstrating our diagnosis scheme for AI class systems.

12 mod 24 Weyl points in the BZ after considering all the symmetry operators of #216, especially C_3 symmetry around the (111) direction. A detailed calculation confirms that there are 12 robust Weyl points related to each other by symmetries at around 3.22 THz, confined on the $k_1 = 0, k_2 = 0,$ and $k_3 = 0$ planes.

We note that 12 Weyl phonons at around 3.22 THz are ideal ones, which are related to each other by symmetries and have equal energies, as shown in Fig. 3(d). There are another 12 Weyl phonons at around 2.58 THz, with the same indicator $z_2 = 1$ for the subgroup #82. Surface states and surface arcs for Weyl phonons are discussed in the Supplemental Material [7].

Diagnosis process for ZrSiO. ZrSiO has a centrosymmetric structure with space group $P4/nmm$ (#129) [57], as shown in Fig. 4(a). ZrSiO is a nodal-line semimetal for electronic structures when the spin-orbit coupling is ignored [20] and features the same topological properties for phonon spectra. Figure 4(b) shows the phonon bands for ZrSiO, which have several band crossings at around 13 THz along several high-symmetry lines. We will discuss what they are, and whether they are topologically protected in the following.

After obtaining the symmetry data for phonons by density-function perturbation theory in step I, we find out that they do not satisfy the CC along Γ -X, Γ -M, Z-A, and Z-R directions for the 14 lowest bands in step II. Violation of CC indicates that a band degeneracy will exist between the 14th and 15th bands at those four high-symmetry lines, which also means that we can use the recursive algorithm to figure out the complete topological information for the degeneracies. In step III, we find that the maximum subgroups satisfying INDC and CC are #81 and #2 after iterating several times. Here, we would like to note that #81 and #2 belong to different “tree branches,” which means that neither of them is a subgroup of the other one.

The indicator group for #81 is $\mathbb{Z}_2 \times \mathbb{Z}_2$, and the corresponding topological invariants for phonons in ZrSiO are (00). Even though the topological invariants are zero, they can still tell us that there will be 0 mod 8 band crossings at both the $k_z = 0$ plane and the $k_z = \pi$ plane. As shown in Fig. 4(d), band crossings are marked by pentagrams. Since $(\mathcal{PT})^2 = +1$ in ZrSiO, all the band crossings must belong to nodal lines/rings. Therefore a possible configuration for the band degeneracies in ZrSiO diagnosed by #81 is 0 mod

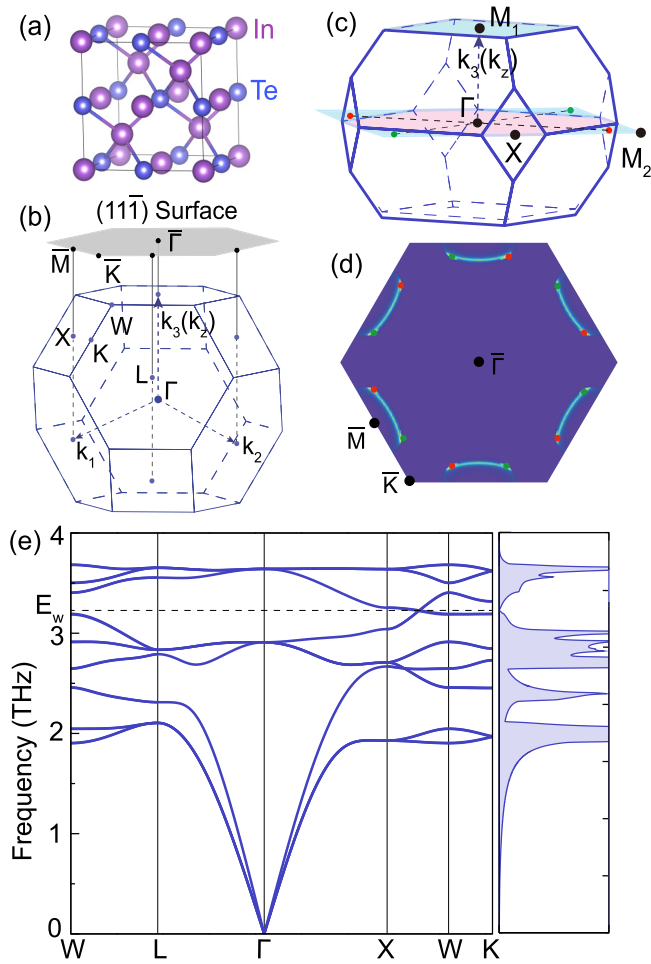


FIG. 3. (a) Crystal structure for In_2Te . (b) Brillouin zone and surface Brillouin zone along the $(11\bar{1})$ direction for #216. (c) Brillouin zone for #82. (d) Distribution for 12 ideal Weyl points between the sixth and seventh phonon bands in the surface Brillouin zone at E_w , where green dots represent Weyl points with Chern number of -1 and red dots represent Weyl points with Chern number of $+1$. (e) Phonon spectra for In_2Te .

8 nodal lines crossing both the $k_z = 0$ plane and the $k_z = \pi$ plane along the (001) direction, as shown in Fig. 4(d).

The indicator group for #2 is $\mathbb{Z}_2 \times \mathbb{Z}_2 \times \mathbb{Z}_2 \times \mathbb{Z}_4$, and the corresponding topological invariants are (0012) for phonons in ZrSiO . Those nonzero indicators tell us another possible configuration for the topological degeneracies in BZ, and we offer two different perspectives to understand it. (i) Because indicator groups are Abelian groups, indicators satisfy the sum rule. Thus (0012) can be written as $(0001) + (0011)$, which indicates a single nodal ring around the Γ and Z points by Ref. [6], respectively. M_z symmetry in ZrSiO will restrict those two nodal rings in the $k_z = 0$ and $k_z = \pi$ plane, which corresponds to the configuration shown in Fig. 4(e). (ii) $z_2 = 1$ and $z_4 = 2$ indicate that any curved surface in the BZ passing Γ , X , and M points (or R , A , and Z points) will be crossed by nodal lines $2 \bmod 4$ times. Therefore one possible configuration is one nodal ring lying on the $k_z = 0$ and $k_z = \pi$ plane, respectively, which also matches Fig. 4(e) well.

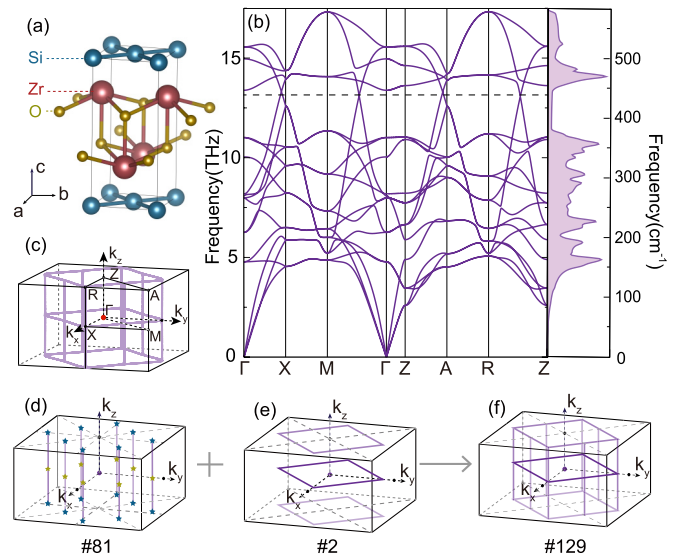


FIG. 4. (a) Crystal structure, (b) phonon spectra, and (c) Brillouin zone for ZrSiO . Purple lines in (c) are nodal lines calculated by first-principles calculations. (d)–(f) are the predicted configurations for node-line degeneracies between the 14th and 15th phonon bands by our algorithm. All the nodal lines carry a quantized π Berry phase.

In the last step, we can get the complete configuration for topological degeneracies in BZ by combining the indicators of subgroup #81 and #2. First-principles calculations show that there are ten nodal lines including two nodal rings in the BZ, i.e., node-cage degeneracies shown in Fig. 4(c), which perfectly matches the diagnosing results in Fig. 4(f).

Conclusion. We designed a recursive algorithm for diagnosing the complete information of topological degeneracies crossing high-symmetry lines by using the indicators of maximum subgroups. This recursive algorithm can be used in any system with $\mathcal{T}^2 = +1$ and compensates for the shortcomings of the previous method, which can only be used in systems satisfying compatibility conditions, i.e., no band degeneracies at high-symmetry points or along high-symmetry lines. In two examples for phonon bands, i.e., In_2Te and ZrSiO , we diagnosed all the topological degeneracies in the Brillouin zone successfully, which verifies the effectiveness of the diagnosing method.

Acknowledgments. T.T.Z. and S.M. acknowledge support from Tokodai Institute for Element Strategy (TIES) funded by MEXT Elements Strategy Initiative to Form Core Research Center. C.F. acknowledges support from the Ministry of Science and Technology of China under Grants No. 2016YFA0302400, No. 2016YFA0300600, and No. 2018YFA0305700; the National Science Foundation of China under Grants No. 11674370, No. 11421092, and No. 11674369; and the Chinese Academy of Sciences under Grants No. XXH13506-202, No. XDB07020100, and No. XDB28000000. L.L. is supported by the National Key R&D Program of China under Grants No. 2017YFA0303800 and No. 2016YFA0302400 and the NSFC under Project No. 11721404. H.M.W. and Z.F. acknowledge support from the Ministry of Science and Technology of China under Grants No. 2016YFA0300600, No. 2016YFA0302400, and

No. 2018YFA0305700; the National Natural Science Foundation under Grants No. 11674370, No. 11421092, and No.

11674369; and the Chinese Academy of Sciences under Grants No. XDB28000000 and No. XXH13506-202.

- [1] H. C. Po, A. Vishwanath, and H. Watanabe, Symmetry-based indicators of band topology in the 230 space groups, *Nat. Commun.* **8**, 50 (2017).
- [2] B. Bradlyn, L. Elcoro, J. Cano, M. G. Vergniory, Z. Wang, C. Felser, M. I. Aroyo, and B. A. Bernevig, Topological quantum chemistry, *Nature (London)* **547**, 298 (2017).
- [3] X.-L. Qi and S.-C. Zhang, Topological insulators and superconductors, *Rev. Mod. Phys.* **83**, 1057 (2011).
- [4] C. L. Kane and T. C. Lubensky, Topological boundary modes in isostatic lattices, *Nat. Phys.* **10**, 39 (2014).
- [5] Z. Song, T. Zhang, Z. Fang, and C. Fang, Quantitative mappings between symmetry and topology in solids, *Nat. Commun.* **9**, 3530 (2018).
- [6] Z. Song, T. Zhang, and C. Fang, Diagnosis for Nonmagnetic Topological Semimetals in the Absence of Spin-Orbital Coupling, *Phys. Rev. X* **8**, 031069 (2018).
- [7] See Supplemental Material at <http://link.aps.org/supplemental/10.1103/PhysRevResearch.2.022066> for (i) definition of compatibility condition, (ii) discussions on the algorithm in spinful systems, and (iii) surface states and arcs for the Weyl phonons at 2.58 THz.
- [8] T. Zhang, Y. Jiang, Z. Song, H. Huang, Y. He, Z. Fang, H. Weng, and C. Fang, Catalogue of topological electronic materials, *Nature (London)* **566**, 475 (2019).
- [9] M. G. Vergniory, L. Elcoro, C. Felser, N. Regnault, B. A. Bernevig, and Z. Wang, A complete catalogue of high-quality topological materials, *Nature (London)* **566**, 480 (2019).
- [10] F. Tang, H. C. Po, A. Vishwanath, and X. Wan, Comprehensive search for topological materials using symmetry indicators, *Nature (London)* **566**, 486 (2019).
- [11] H. Weng, C. Fang, Z. Fang, B. A. Bernevig, and X. Dai, Weyl Semimetal Phase in Noncentrosymmetric Transition-Metal Monophosphides, *Phys. Rev. X* **5**, 011029 (2015).
- [12] C. Fang, M. J. Gilbert, X. Dai, and B. A. Bernevig, Multi-Weyl Topological Semimetals Stabilized by Point Group Symmetry, *Phys. Rev. Lett.* **108**, 266802 (2012).
- [13] G. Xu, H. Weng, Z. Wang, X. Dai, and Z. Fang, Chern Semimetal and the Quantized Anomalous Hall Effect in HgCr_2Se_4 , *Phys. Rev. Lett.* **107**, 186806 (2011).
- [14] S.-M. Huang, S.-Y. Xu, I. Belopolski, C.-C. Lee, G. Chang, T.-R. Chang, B. Wang, N. Alidoust, G. Bian, and M. Neupane *et al.*, New type of Weyl semimetal with quadratic double Weyl fermions, *Proc. Natl. Acad. Sci. USA* **113**, 1180 (2016).
- [15] B. Bradlyn, J. Cano, Z. Wang, M. G. Vergniory, C. Felser, R. J. Cava, and B. A. Bernevig, Beyond Dirac and Weyl fermions: Unconventional quasiparticles in conventional crystals, *Science* **353**, aaf5037 (2016).
- [16] Z. Wang, H. Weng, Q. Wu, X. Dai, and Z. Fang, Three-dimensional Dirac semimetal and quantum transport in Cd_3As_2 , *Phys. Rev. B* **88**, 125427 (2013).
- [17] Z. Wang, Y. Sun, X.-Q. Chen, C. Franchini, G. Xu, H. Weng, S. X. Dai, and Z. Fang, Dirac semimetal and topological phase transitions in $A_3\text{Bi}$ ($A = \text{Na, K, Rb}$), *Phys. Rev. B* **85**, 195320 (2012).
- [18] Z. K. Liu, B. Zhou, Y. Zhang, Z. J. Wang, H. M. Weng, D. Prabhakaran, S.-K. Mo, Z. X. Shen, Z. Fang, X. Dai *et al.*, Discovery of a three-dimensional topological Dirac semimetal, Na_3Bi , *Science* **343**, 864 (2014).
- [19] R. M. Geilhufe, S. S. Borysov, A. Bouhon, and A. V. Balatsky, Data mining for three-dimensional organic Dirac materials: Focus on space group 19, *Sci. Rep.* **7**, 7298 (2017).
- [20] Q. Xu, Z. Song, S. Nie, H. Weng, Z. Fang, and Xi Dai, Two-dimensional oxide topological insulator with iron-pnictide superconductor LiFeAs structure, *Phys. Rev. B* **92**, 205310 (2015).
- [21] C. Fang, H. Weng, Xi Dai, and Z. Fang, Topological nodal line semimetals, *Chin. Phys. B* **25**, 117106 (2016).
- [22] B. Lv, H. M. Weng, B. B. Fu, X. P. Wang, H. Miao, J. Ma, P. Richard, X. C. Huang, L. X. Zhao, G. F. Chen *et al.*, Experimental Discovery of Weyl Semimetal TaAs, *Phys. Rev. X* **5**, 031013 (2015).
- [23] S.-Y. Xu, I. Belopolski, N. Alidoust, M. Neupane, G. Bian, C. Zhang, R. Sankar, G. Chang, Z. Yuan, C.-C. Lee *et al.*, Discovery of a Weyl Fermion semimetal and topological Fermi arcs, *Science* **349**, 613 (2015).
- [24] X. Wan, A. M. Turner, A. Vishwanath, and S. Y. Savrasov, Topological semimetal and Fermi-arc surface states in the electronic structure of pyrochlore iridates, *Phys. Rev. B* **83**, 205101 (2011).
- [25] W. Chen, M. Xiao, and C. Chan, Photonic crystals possessing multiple Weyl points and the experimental observation of robust surface states, *Nat. Commun.* **7**, 13038 (2016).
- [26] D. T. Son and B. Z. Spivak, Chiral anomaly and classical negative magnetoresistance of Weyl metals, *Phys. Rev. B* **88**, 104412 (2013).
- [27] X. Huang, L. Zhao, Y. Long, P. Wang, D. Chen, Zhanhai Yang, H. Liang, M. Xue, H. Weng, Z. Fang *et al.*, Observation of the Chiral-Anomaly-Induced Negative Magnetoresistance in 3D Weyl Semimetal TaAs, *Phys. Rev. X* **5**, 031023 (2015).
- [28] J. Xiong, S. K. Kushwaha, T. Liang, J. W. Krizan, M. Hirschberger, W. Wang, R. J. Cava, and N. P. Ong, Evidence for the chiral anomaly in the Dirac semimetal Na_3Bi , *Science* **350**, 413 (2015).
- [29] A. A. Zyuzin and A. A. Burkov, Topological response in Weyl semimetals and the chiral anomaly, *Phys. Rev. B* **86**, 115133 (2012).
- [30] H. B. Nielsen and M. Ninomiya, The adler-bell-jackiw anomaly and weyl fermions in a crystal, *Phys. Lett. B* **130**, 389 (1983).
- [31] L. Lu, J. D. Joannopoulos, and M. Soljačić, Topological photonics, *Nat. Photonics* **8**, 821 (2014).
- [32] L. Lu, J. D. Joannopoulos, and M. Soljačić, Topological states in photonic systems, *Nat. Phys.* **12**, 626 (2016).
- [33] L. Lu, Z. Wang, D. Ye, L. Ran, L. Fu, J. D. Joannopoulos, and M. Soljačić, Experimental observation of Weyl points, *Science* **349**, 622 (2015).

- [34] T. Zhang, Z. Song, A. Alexandradinata, H. Weng, C. Fang, L. Lu, and Z. Fang, Double-Weyl Phonons in Transition-Metal Monosilicides, *Phys. Rev. Lett.* **120**, 016401 (2018).
- [35] H. Miao, T. T. Zhang, L. Wang, D. Meyers, A. H. Said, Y. L. Wang, Y. G. Shi, H. M. Weng, Z. Fang, and M. P. M. Dean, Observation of Double Weyl Phonons in Parity-Breaking FeSi, *Phys. Rev. Lett.* **121**, 035302 (2018).
- [36] R. Fleury, A. B. Khanikaev, and A. Alù, Floquet topological insulators for sound, *Nat. Commun.* **7**, 11744 (2016).
- [37] S. H. Mousavi, A. B. Khanikaev, and Z. Wang, Topologically protected elastic waves in phononic metamaterials, *Nat. Commun.* **6**, 8682 (2015).
- [38] B. Gin-ge Chen, N. Upadhyaya, and V. Vitelli, Nonlinear conduction via solitons in a topological mechanical insulator, *Proc. Natl. Acad. Sci. USA* **111**, 13004 (2014).
- [39] R. Süssstrunk and S. D. Huber, Observation of phononic helical edge states in a mechanical topological insulator, *Science* **349**, 47 (2015).
- [40] L. M. Nash, D. Kleckner, A. Read, V. Vitelli, A. M. Turner, and W. T. M. Irvine, Topological mechanics of gyroscopic metamaterials, *Proc. Natl. Acad. Sci. USA* **112**, 14495 (2015).
- [41] D. Z. Rocklin, B. Gin-ge Chen, M. Falk, V. Vitelli, and T. C. Lubensky, Mechanical Weyl Modes in Topological Maxwell Lattices, *Phys. Rev. Lett.* **116**, 135503 (2016).
- [42] Z. Yang, F. Gao, X. Shi, X. Lin, Z. Gao, Y. Chong, and B. Zhang, Topological Acoustics, *Phys. Rev. Lett.* **114**, 114301 (2015).
- [43] C. He, X. Ni, H. Ge, X.-C. Sun, Y.-B. Chen, M.-H. Lu, X.-P. Liu, and Y.-F. Chen, Acoustic topological insulator and robust one-way sound transport, *Nat. Phys.* **12**, 1124 (2016).
- [44] S. D. Huber, Topological mechanics, *Nat. Phys.* **12**, 621 (2016).
- [45] R. Süssstrunk and S. D. Huber, Classification of topological phonons in linear mechanical metamaterials, *Proc. Natl. Acad. Sci. USA* **113**, E4767 (2016).
- [46] W.-C. Ji and J.-R. Shi, Topological phonon modes in a two-dimensional Wigner crystal, *Chin. Phys. Lett.* **34**, 036301 (2017).
- [47] Y. Liu, Y. Xu, S.-C. Zhang, and W. Duan, Model for topological phononics and phonon diode, *Phys. Rev. B* **96**, 064106 (2017).
- [48] B. W. Xia, R. Wang, Z. J. Chen, Y. J. Zhao, and H. Xu, Symmetry-Protected Ideal Type-II Weyl Phonons in CdTe, *Phys. Rev. Lett.* **123**, 065501 (2019).
- [49] K. Li, C. Li, J. Hu, Y. Li, and C. Fang, Dirac and Nodal Line Magnons in Three-Dimensional Antiferromagnets, *Phys. Rev. Lett.* **119**, 247202 (2017).
- [50] W. Yao, C. Li, L. Wang, S. Xue, Y. Dan, K. Iida, K. Kamazawa, K. Li, C. Fang, and Y. Li, Topological spin excitations in a three-dimensional antiferromagnet, *Nat. Phys.* **14**, 1011 (2018).
- [51] A. P. Schnyder, S. Ryu, A. Furusaki, and A. W. W. Ludwig, Classification of topological insulators and superconductors in three spatial dimensions, *Phys. Rev. B* **78**, 195125 (2008).
- [52] C.-K. Chiu, J. C. Y. Teo, A. P. Schnyder, and S. Ryu, Classification of topological quantum matter with symmetries, *Rev. Mod. Phys.* **88**, 035005 (2016).
- [53] S. Ryu, A. P. Schnyder, A. Furusaki, and A. W. W. Ludwig, Topological insulators and superconductors: Tenfold way and dimensional hierarchy, *New J. Phys.* **12**, 065010 (2010).
- [54] G. A. Gamal, A. T. Nagat, M. M. Nassary, and A. M. Abou-Alwafa, Some physical properties of Ga₂Se single crystals, *Cryst. Res. Technol.* **31**, 359 (1996).
- [55] X. Gonze and C. Lee, Dynamical matrices, born effective charges, dielectric permittivity tensors, and interatomic force constants from density-functional perturbation theory, *Phys. Rev. B* **55**, 10355 (1997).
- [56] G. Kresse and J. Furthmüller, Efficient iterative schemes for *ab initio* total-energy calculations using a plane-wave basis set, *Phys. Rev. B* **54**, 11169 (1996).
- [57] H. Onken, K. Vierheilg, and H. Hahn, Über silicid-und germanidchalkogenide des zirkons und hafniums, *Z. Anorg. Allg. Chem.* **333**, 267 (1964).

Diagnosis scheme for topological degeneracies crossing high-symmetry lines

Tiantian Zhang,^{1,2,3} Ling Lu,^{1,4} Shuichi Murakami,^{2,3} Zhong Fang,^{1,5} Hongming Weng,^{1,5} and Chen Fang^{1,6}

¹*Institute of Physics, Chinese Academy of Sciences/Beijing National
Laboratory for Condensed Matter Physics, Beijing 100190, China*

²*Department of Physics, Tokyo Institute of Technology, Ookayama, Meguro-ku, Tokyo 152-8551, Japan*

³*Tokodai Institute for Element Strategy, Tokyo Institute of Technology,
Nagatsuta, Midori-ku, Yokohama, Kanagawa 226-8503, Japan*

⁴*Songshan Lake Materials Laboratory, Dongguan, Guangdong 523808, China*

⁵*Collaborative Innovation Center of Quantum Matter, Beijing, 100084, China*

⁶*CAS Center for Excellence in Topological Quantum Computation, Beijing 100190, China*

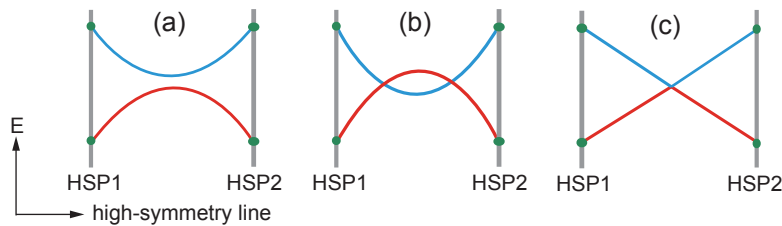


FIG. 1. Three kinds of band connection along a high-symmetry line. (a-b) are both the cases that satisfy compatibility condition, and (c) is the case that violate it.

I. CALCULATION METHODS

In this paper, phonon dispersions of ZrSiO and In₂Te are calculated by Vienna *ab initio* simulation package (VASP), based on density functional perturbation theory (DFPT). Exchange-correlation potential is treated within the generalized gradient approximation (GGA) of Perdew-Burke-Ernzerhof type. The wave functions are expanded in plane waves with a kinetic energy cutoff of 400 eV and a sum on a Monkhorstpack grid of $4 \times 4 \times 4$ k points for integrals over the BZ for a $3 \times 3 \times 3$ supercell approach for both ZrSiO and In₂Te. The crystal structure has been fully relaxed until the residual force on each atom is less than $0.001 \text{ eV}/\text{\AA}$ before the phonon spectra calculation. Chern numbers of the Weyl points are calculated by Wilson loop method. The second-order tensor of the force constant including the non-analytical term in Cartesian coordinates is calculated for the first step, then the Green's function is used to obtain the surface local density of states[1–3].

II. COMPATIBILITY CONDITION

Compatibility condition only depends on the number of irreps for the occupied bands at high-symmetry points, which means this condition can only tell us the band connection between high-symmetry points, *i.e.*, diagnosing whether there is a band crossing along high-symmetry lines or not. Thus, if the symmetry data at high-symmetry points satisfy the compatibility condition, then there will be no band inversions along high-symmetry lines, as shown in Fig. 1(a). However, if there is one, the band inversion can be gapped out with a perturbation, as shown in Fig. 1(b). If the symmetry data at high-symmetry points doesn't satisfy the compatibility condition, then there must be a topological band crossing along a high-symmetry line, as shown in Fig. 1(c).

For example, SrSi₂[4] is a Weyl semimetal having a band inversion like Fig. 1(b) along Γ -X direction. Although the symmetry data for SrSi₂ satisfies the compatibility condition, however, it is a topological semimetal instead of trivial states. In both our manuscript and the previous symmetry-based indicator theories, “gapped trivial phase” means that all the band crossings can be gapped out without changing the order of irreps between the occupied bands and unoccupied bands at high-symmetry momenta, no matter how large the perturbation will be. Thus, SrSi₂ will be diagnosed as a trivial insulator because the band inversion along Γ -X direction can be gapped out without changing the order of irreps at high-symmetry points.

III. FURTHER DISCUSSIONS ON THE ALGORITHM

Here we would like to discuss more on the case where #1 will be the end. Before the discussion, we note that, even a zero symmetry-based indicator is obtained in step IV, we should continue to step V instead of going back to step III.

There are six space groups that will end up with #1 if the compatibility condition is violated, because they only have one operator generator. Those six space groups are #3 and #5 (which only have a C₂ rotation symmetry), #6 and #8 (which only have a mirror symmetry), #143 and #146 (which only have a C₃ rotation symmetry). Space group #2 also only have one generator, which is inversion symmetry, however, compatibility for #2 is always satisfied regardless of the irreducible representations (irreps) at high-symmetry momenta. Thus, topological degeneracies in #2 can always diagnosed by symmetry-based indicator.

For example, we consider a material with space group #6, which only has a mirror symmetry. According to our algorithm, if the symmetry data violates the compatibility condition in step II, we should use the subgroup for further

Point Group	LA irreps	TA irreps	Point Group	LA irreps	TA irreps
C_1	/	/	D_2	B_1	B_2, B_3
C_2	A	B, B	D_3	A_2	E
C_3	A	E	D_4	A_2	E
C_4	A	E	D_6	A_2	E_1
C_6	A	E'	D_{2d}	B_2	E
C_{2v}	A_1	B_1, B_2	D_{3d}	A_{2u}	E_u
C_{3v}	A_1	E	C_{1h}	A''	A', A'
C_{4v}	A_1	E	C_{2h}	A_u	B_u, B_u
C_{6v}	A_1	E_1	C_{3h}	A''	E'
D_{2h}	B_{1u}	B_{2u}, B_{3u}	C_{4h}	A_u	${}^1E_u + {}^2E_u$
D_{3h}	A_2''	E'	C_{6h}	A_u	${}^1E_u + {}^2E_u$
D_{4h}	A_{2u}	E_u	T		T
D_{6h}	A_{2u}	E_{1u}	T_h		T_u
S_2	A_u	A_u, A_u	O		T_1
S_4	B	E	T_d		T_2
S_6	A_u	${}^1E_u, {}^2E_u$	O_h		T_{1u}

TABLE I. Irreducible representations of acoustic phonon branches at Γ point for 32 point groups. LA stands for a longitudinal acoustic branch, while TA stands for a transverse acoustic branch.

diagnosis in step III. However, because the space group #1 is the only subgroup of #6, this case is classified as “topological degeneracies diagnosed by compatibility condition”. This occurs when there is a nodal line/ring on a mirror plane. Other cases of “topological degeneracies diagnosed by compatibility condition” is the Weyl points on a C_2/C_3 -axis protected by the C_2/C_3 symmetry.

Algorithm proposed in this paper can also be applied to other symmetry classes, such as class AII with spin-orbit coupling. In class AII, we just need to replace the indicator formulae into spinful ones in step IV, and we can obtain trivial/topological (crystalline) insulator states in the last step. For example, Na_3Bi with the space group #194 is a famous Dirac semimetal protected by time-reversal symmetry and C_3 symmetry, and the symmetry data will break compatibility condition in step II. By ignoring the C_3 symmetry in step III, we will obtain a subgroup with #12. Indicators for subgroup #12 are $z_2 z_2 z_4 = (003)$, which corresponds to a topological insulator, meaning that breaking C_3 symmetry will lead to a topological phase transition to a topological insulator. Such kind of diagnosing process in class AII starting from a topological semimetal and ending with a trivial/topological (crystalline) insulator, will offer a way to modulate topological phase transitions for experiments.

We also would like to note that not all gapped phases protected by the subgroup H will be forbidden by the space group G , even though sometimes we can obtain a gapped phase for H when there is a band inversion in G . For example, Bi_2Se_3 with space group #166 is a topological insulator, which will still be a topological insulator if we break the C_3 symmetry and have a subgroup #2. Thus, Bi_2Se_3 is a material where a gapped phase will exist in both the subgroup H and the space group G .

IV. IRREDUCIBLE REPRESENTATIONS FOR ACOUSTIC PHONONS AT Γ POINT

A phonon is one of the widely studied particles in AI class systems. In three dimensional (3D) phonon systems, three acoustic phonons are degenerated since they are Goldstone excitations, and have specific irreducible representations once we know the symmetries of the system. In particular, the little group at the Γ point is equal to a point group, so there are only 32 kinds of Goldstone modes for 3D materials. All the irreducible representations of acoustic phonons for each point group are listed in Table. I.

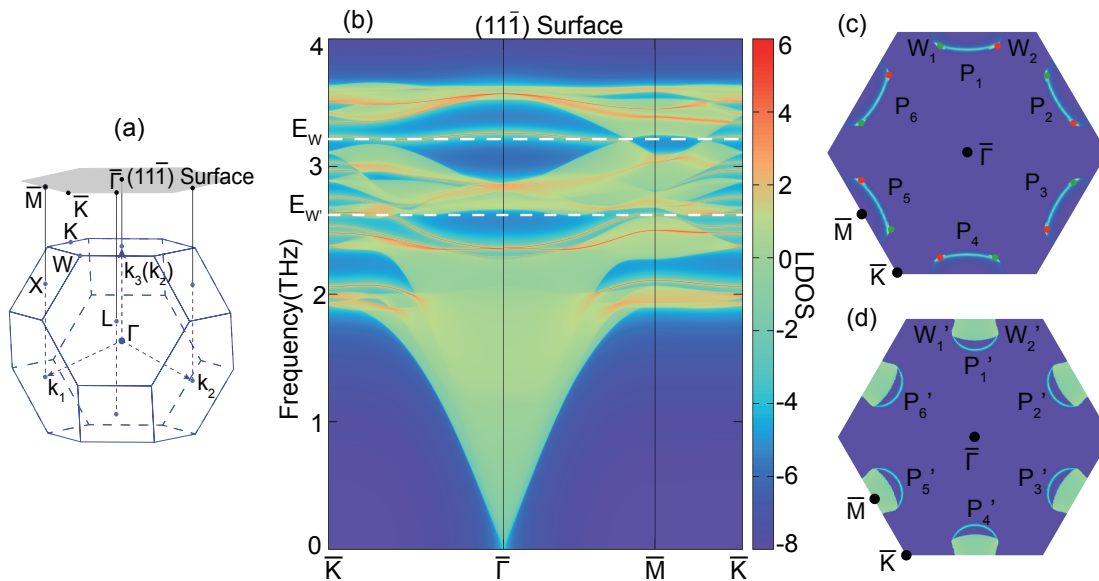


FIG. 2. (a) Brillouin zone and surface Brillouin zone along $(11\bar{1})$ direction for In_2Te . (b) Surface states for In_2Te along $(11\bar{1})$ direction. (c) Iso-energetic surface for In_2Te at 3.22THz along $(11\bar{1})$ direction. (d) Iso-energetic surface for In_2Te at 2.58THz along $(11\bar{1})$ direction.

V. SURFACE STATES AND ARCS FOR IN_2TE AT 3.22THZ AND 2.58THZ

Helical and topological one-way surface states are unique features for Weyl materials, which is distinguished from topologically trivial materials. The helical surface states will develop into an open surface arc when we draw an isoenergetic surface in the surface BZ, whose ends are pinned to the projection of Weyl points from the 3D BZ. To gain more insight of its topological nature, we calculate the local density states and the iso-frequency surface contours on the $(11\bar{1})$ surface in Fig. 2 (b-c) and on the (111) surface in Fig. 2 (d).

Symmetries left on the $(11\bar{1})$ surface are three-fold rotation symmetry along (111) direction 3_{111}^+ , mirror symmetry perpendicular to (011) direction m_{011} , and time-reversal symmetry T , which makes a hexagonal surface BZ along $(11\bar{1})$ direction shown in grey in Fig. 2(a). For the ideal Weyl phonons at around 3.22 THz (E_W), one Weyl phonon with right-hand chirality is projected onto W_2 , and another Weyl phonon with left-hand chirality is projected onto W_1 , as shown in Fig. 2(c). This pair of Weyl phonons, called P_1 , are connected by m_{011} symmetry. Other two pairs of Weyl phonons P_3, P_5 are related to P_1 by 3_{111}^+ symmetry, and those three pairs of Weyl phonons are associated with the other three pairs by \mathcal{T} , just like Fig. 2(c). Each surface arc connects two Weyl points with opposite chirality and constrained by $3_{111}^+, m_{011}$, and \mathcal{T} in the surface BZ. Both the density of states for the bulk phonons in the main text and the clean iso-energetic surface in Fig. 2(c) prove that phonons at E_W are ideal Weyl phonons without coexisting trivial surface states or bulk dispersions.

Figure 2(d) shows the positions of 12 Weyl points at around 2.58THz ($E_{W'}$) along (111) direction. Symmetries left on the (111) surface are the same as $(11\bar{1})$ surface. However, the iso-energetic contour shows that 12 Weyl phonons at $E_{W'}$ is not clean due to the existence of bulk pockets. In addition, the distribution of the six pairs of Weyl points and associated surface arcs are exactly the same with the other six pairs at E_W .

VI. WEYL POSITIONS FOR IN_2TE AT 3.22THZ AND 2.58THZ

We list all the positions for Weyl phonons at both 3.22THz and 2.58THz. The fractional coordinate $\mathbf{k}_j = 0.5 - \mathbf{k}_i = 0.1334$ is for the six pairs of Weyl points at E_W , and $\mathbf{k}_j = 0.5 - \mathbf{k}_i = 0.0986$ is for the other six pairs of Weyl points at $E_{W'}$.

-
- [1] M. P. Lopez Sancho, J. M. Lopez Sancho, J. M. L. Sancho, and J. Rubio. Highly convergent schemes for the calculation of bulk and surface Green functions. *Journal of Physics F Metal Physics*, 15:851–858, April 1985.
- [2] M P Lopez Sancho, J M Lopez Sancho, and J Rubio. Quick iterative scheme for the calculation of transfer matrices: application to mo (100). *Journal of Physics F: Metal Physics*, 14(5):1205, 1984.
- [3] QuanSheng Wu, ShengNan Zhang, Hai-Feng Song, Matthias Troyer, and Alexey A Soluyanov. Wanniertools: An open-source software package for novel topological materials. *Computer Physics Communications*, 224:405–416, 2018.
- [4] Shin-Ming Huang, Su-Yang Xu, Ilya Belopolski, Chi-Cheng Lee, Guoqing Chang, Tay-Rong Chang, BaoKai Wang, Nasser Alidoust, Guang Bian, Madhab Neupane, et al. New type of Weyl semimetal with quadratic double Weyl Fermions. *Proceedings of the National Academy of Sciences*, 113(5):1180–1185, 2016.

Weyl Name	W_1	W_2	W_3	W_4	W_5	W_6
Position in 3D BZ	$(-\mathbf{k}_i, 0.5, \mathbf{k}_j)$	$(0.5, -\mathbf{k}_i, \mathbf{k}_j)$	$(0.5, -\mathbf{k}_j, -\mathbf{k}_i)$	$(-\mathbf{k}_i, \mathbf{k}_j, 0.5)$	$(-\mathbf{k}_j, \mathbf{k}_i, 0.5)$	$(\mathbf{k}_j, 0.5, \mathbf{k}_i)$
Weyl Name	W_7	W_8	W_9	W_{10}	W_{11}	W_{12}
Position in 3D BZ	$(\mathbf{k}_i, 0.5, -\mathbf{k}_j)$	$(0.5, \mathbf{k}_i, -\mathbf{k}_j)$	$(0.5, \mathbf{k}_j, \mathbf{k}_i)$	$(\mathbf{k}_i, -\mathbf{k}_j, 0.5)$	$(\mathbf{k}_j, -\mathbf{k}_i, 0.5)$	$(-\mathbf{k}_j, 0.5, -\mathbf{k}_i)$

TABLE II. Weyl positions in the 3D BZ. .